npj | 2D materials and applications

www.nature.com/npj2dmaterials

ARTICLE OPEN

Check for updates

Essential role of momentum-forbidden dark excitons in the energy transfer responses of monolayer transition-metal dichalcogenides

Jhen-Dong Lin[1], Ping-Yuan Lo[1], Guan-Hao Peng[1], Wei-Hua Li[1], Shiang-Yu Huang[2], Guang-Yin Chen[3] and Shun-Jen Cheng[1]✉

We present a theoretical investigation of exciton-mediated Förster resonant energy transfers (FRET's) from photoexcited quantum dots (QD's) to transition-metal dichalcogenide monolayers (TMD-ML's), implemented by the quantum theory of FRET on the base of first-principles-calculated exciton fine structures. With the enhanced electron-hole Coulomb interactions, atomically thin TMD-MLs are shown to serve as an exceptional platform for FRET that are mediated purely by excitons and take full advantage of the superior excitonic properties. Remarkably, the energy-transfer responses of atomically thin TMD-ML's are shown to be dictated by the momentum-forbidden dark excitons rather than the commonly recognized bright ones. Specifically, the longitudinal dark exciton states following the exchange-driven light-like linear band dispersion play a key role in grading up the efficiency and robustness of FRET of TMD-ML against the inhomogeneity of QD-donor ensembles. With the essential involvement of dark excitons, the FRET responses of TMD-ML's no longer follow the distance power law as classically predicted and, notably, cannot manifest the dimensionality of the donor-acceptor system.

npj 2D Materials and Applications (2023)7:51 ; https://doi.org/10.1038/s41699-023-00414-z

INTRODUCTION

Förster resonant energy transfer (FRET) is a non-radiative electromagnetic process that, via non-contact near field coupling, enables the transfer of excitation energy from a photo-excited object (donor) to another unexcited one (acceptor) in close proximity (typically apart by a distance of few to tens of nm)[1–5]. Since FRET is not a radiative process mediated by real photons, the rate of FRET is not restricted by the slow spontaneous radiative decay of the donor and finite optical cross section of the acceptor. Inspired by efficient excitonic energy transfer in botanical photosynthesis revealed by early studies[6–11], the FRET mediated with exciton is considered as an alternative route for grading up solid-state photo-voltaic devices by taking advantage of superior oscillator strength of exciton to enhance the light-generation and -harvesting[12–18]. Nowadays, numerous research has been persistently conducted to investigate various emergent opto-electronic materials that are potentially advantageous for the realization of exciton-based FRET[19–40].

Atomically thin transition-metal dichalcogenides (TMD's) are known as excellent opto-electronic materials, in possession of remarkable light-matter interaction and pronounced excitonic properties[41–50]. Due to weak Coulomb screening in low-dimensionality, the inter-particle Coulomb interactions in the 2D materials are greatly enhanced, and the photo-excited electron-hole (*e-h*) pairs in TMD-ML's form tightly bound excitons with giant binding energy over hundreds of meV[51–54]. In fact, TMD monolayers (TMD-ML's) serve as an exceptional and suitable platform for studying exciton-mediated FRET's because the giant binding energy ($\gtrsim 10^2$ meV) of exciton well separates the low-lying exciton states spectrally apart from the free *e-h* pair continuum spectra. Hence, over the wide range of resonance energy (>10^2 meV), the FRET from photo-excited donors to TMD-acceptors can be mediated only by excitons to take full advantage of the superior excitonic properties of TMD-ML.

Recent experiments have evidenced the FRET's of TMD-ML's to be extraordinarily fast and show near unity transfer efficiencies[19,26,27,55–57] that far exceed the limited FRET efficiencies of ordinary bulk materials or mesoscopic systems[58,59]. Theoretically, over a decade ago, Swathi and Sebastian[60] showed that the FRET between zero-dimensional (0D) donors and two-dimensional (2D) acceptors separated by a distance d follows the d^{-4} dependence, instead of the d^{-6} distance dependence commonly recognized for 0D-0D systems. In another work published in the same year[61], Swathi and Sebastian addressed the exponential distance dependence of the FRET in a 0D-2D system with very short distances. The theory was later expanded by Malic et al.[62] for molecule-graphene systems, and subsequently extended to graphene-TMD systems[63], which exhibit the exponential distance dependence of FRET. Zhang et al. first pointed out the remarkable effects of dark excitons in the FRET between 1D carbon nanotubes[40]. Very recently, Katzer et al.[64] carried out the theoretical investigation of the momentum-forbidden dark excitons in the FRET between dye molecules and 2D semiconductors using a fully analytical approach and predicted the d^{-4} dependence in the model of 2D material where the electron-hole exchange interaction of exciton is neglected.

In this work, we carry out the theoretical and computational investigation, implemented on the basis of the first principles, of the energy transfer from donors of nanocrystal quantum dots (QD's) to an acceptor of MoS_2 monolayer (MoS_2-ML), one of the best-known TMD-ML's, as schematically illustrated in Fig. 1c. According to the violated optical selection rules, optically inactive excitons are classified as so-called spin-forbidden (SFDX)[65–70] and momentum-forbidden dark exciton (MFDX)[69,71–74]. Besides the confirmation of the previous model predictions of the distance

[1]Department of Electrophysics, National Yang Ming Chiao Tung University, Hsinchu 300, Taiwan. [2]Leibniz Institute of Photonic Technology, Albert-Einstein Straße 9, Jena 07745, Germany. [3]Department of Physics, National Chung Hsing University, Taichung 402, Taiwan. ✉email: sjcheng@nycu.edu.tw

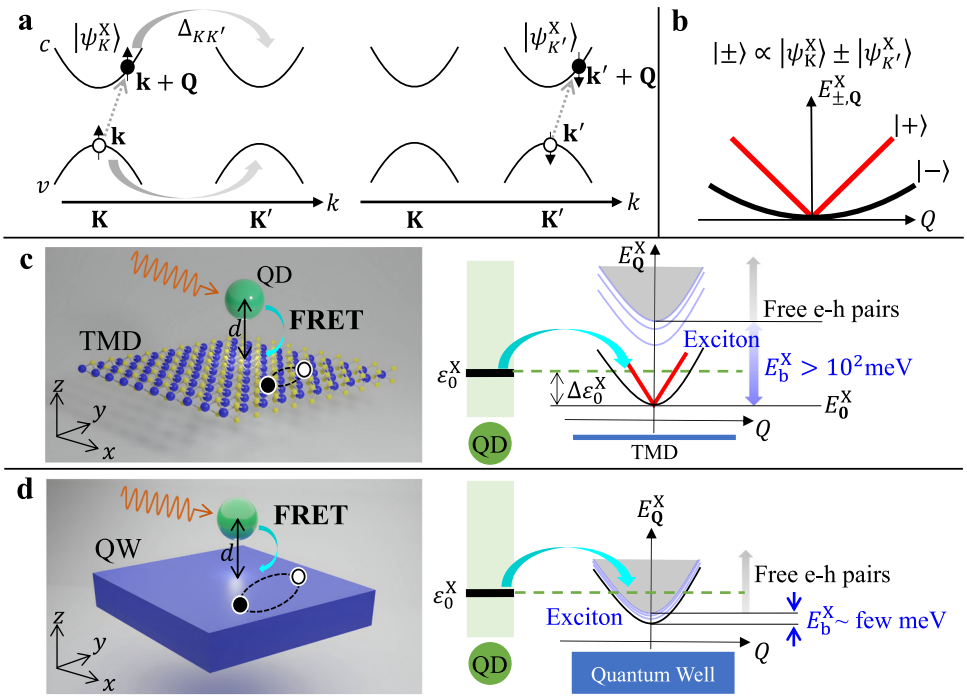

Fig. 1 Schematics of the electronic band structure of a transition-metal dichalcogenide (TMD) monolayer (ML), schematic of exciton band of a TMD-ML, and schematics of the Förster energy transfer systems. a Schematics of valley-characteristic band structure of a TMD-ML. Due to the *e-h* exchange interaction, $\Delta_{K'K}$, a photo-excited inter-band transition in the K-valley exciton with momentum $\hbar\mathbf{Q}$ is intrinsically coupled to that in the K′-valley with the same momentum. **b** The *e-h* exchange interaction leads to the valley-mixing of exciton states and splits the spin-allowed exciton bands of a TMD-ML into a parabolic lower band (black curve) and linear upper one (red curve). **c**, **d** Schematics of the Förster energy transfer systems composed of (**c**) a semiconductor quantum dot (QD) and an atomically thin TMD-ML, and (**d**) a QD and a thick mesoscopic quantum well. In the case of (**c**), the FRET is fully exciton mediated because of the large binding energy ($E_b^X > 10^2$meV) of exciton that well separates the spectra of exciton and non-interacting free *e-h* pairs. By contrast, in the case of (**d**), the excitation energy of the QD yet likely falls in the energy regime of continuum spectrum of *e-h* pairs since the binding energy of exciton in a mesoscopic quantum well is typically only a few meV.

dependences of the FRETs between generic 0D and 2D systems, our first-principles-based computation confirms the essential role of MFDX's in the resonant energy transfer processes of TMD-ML's and reveals the unusual distance dependence of the FRET between inhomogeneous QD donors and a TMD-ML acceptor, deviating from the widely known d^{-4} and exponential distance dependences. More importantly, the presence of the *e-h* exchange interaction in TMD monolayers intermixes exciton states at different valleys, splitting up the exciton bands into the linear and parabolic bands with longitudinal and transverse excitonic dipole orientation[69,75,76]. Consequently, the longitudinal MFDX states of the exchange-resulting light-like linear exciton bands of TMD-ML's play the key role in grading up the efficiency and robustness of FRET against the inhomogeneity of QD-donor ensembles. With the enhanced electron-hole exchange interaction of exciton in anatomically thin TMD-ML acceptors and certain energy variations of inhomogeneous QD donors, we shall show that the FRET between QD's and a TMD-ML is not necessary to follow the commonly recognized d^{-4} or exponential distance dependences, but could exhibit the unusual d^{-5} or even higher order distance dependence.

RESULTS AND DISCUSSION

Valley-characteristic band structures of TMD-ML's

The band structure of TMD-ML is characterized by two distinctive valleys located at the K and K′ corner points of the first Brillouin zone where the direct band gaps in the visible light range are opened[41,77]. As the time-reversal counterparts, the optical transitions between the conduction and valence band extrema in the K- and K′-valleys follow the opposite optical helicity, allowing for the valley-selective photo-excitation by using polarized lights[78–80]. The first-principles-calculated spin and valley-characteristic band structure of a MoS_2-ML is shown in Supplementary Fig. 1a or can be found in many published papers of literature, e.g., refs. [52,77,81–84].

Throughout this work, we focus on the spin-allowed transitions of a MoS_2-ML from the topmost valence band to the spin-like conduction band in the same valley (K or K′), i.e., the spin-allowed intra-valley A exciton[54,85–88], which satisfies the spin selection rule for FRET.

Valley-split exciton band structures of TMD-ML's

Due to enhanced Coulomb interaction in 2D materials, photo-excited electron-hole pairs in a TMD-ML form tightly bound excitons featured with extraordinarily high binding energy over hundreds of meV and giant transition dipoles. As compared with the excitons in bulks or mesoscopic quantum wells, the binding energy of exciton in a TMD-ML is two orders of magnitude larger, and the resulting Bohr radius (merely 1–2 nm) of exciton is one order of magnitude smaller[89,90]. Such a small Bohr radius of exciton in a TMD-ML leads to the giant dipole moment of exciton and superiorly significant light-matter interaction[42,45,47,91].

Moreover, the enhanced electron-hole Coulomb interactions in valley-characteristic TMD-ML's also give rise to efficient inter-valley excitonic couplings that, via the intrinsic *e-h* exchange interaction, intermix the spin-allowed exciton states of distinct valleys[69,75,76,92]. Figure 1a depicts the *e-h* exchange interaction that couples an intra-valley exciton carrying the momentum $\hbar\mathbf{Q}$ in the K-valley to that in the K′-valley. Figure 1b shows the schematics of the low-

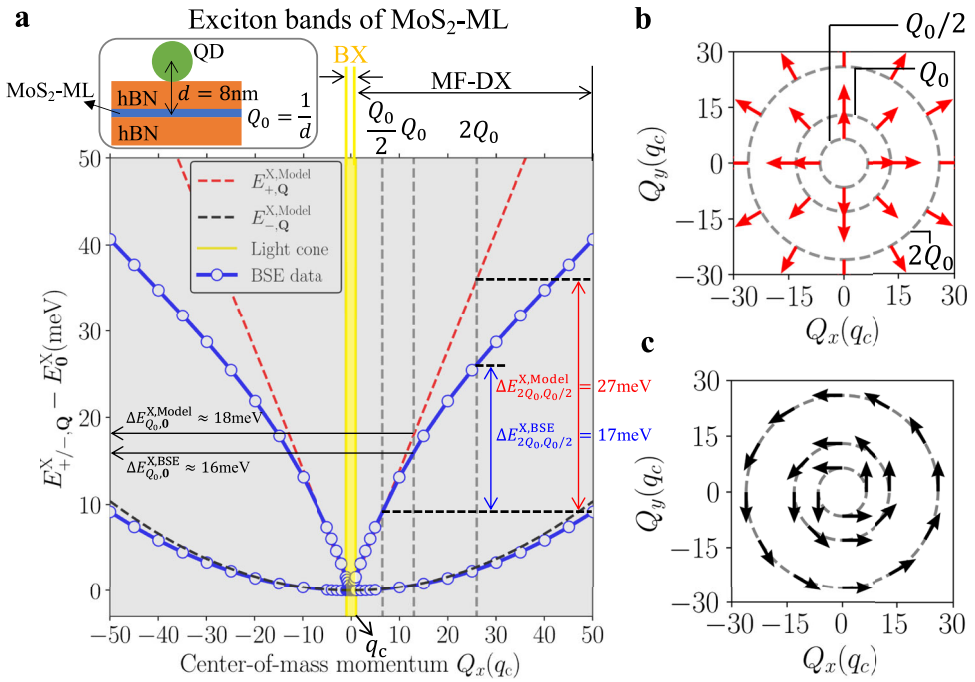

Fig. 2 Valley-split exciton band structure of MoS_2-ML and Q-dependent dipoles of finite momentum exciton states. a Valley-split exciton band structure of MoS_2-ML, composed of both the parabolic lower band (black dashed curve) and linear upper one (red dashed curve) simulated by pseudo-spin model, and calculated by numerically solving the DFT-based Bethe-Salpeter equation (blue curve with hollow marker). The exciton states lying in the small reciprocal area of the light cone where $Q < q_c$ are optically active in the sense of far-field and are called bright excitons (BX's). By contrast, the optically inactive exciton states out of the light cone are referred to as momentum-forbidden dark excitons (MFDX's). Remarkably, the longitudinal exciton states unusually follow a light-like linear dispersion with a steep slope $2\gamma \sim 144$ meV · nm, resulting from the exceptionally pronounced *e-h* exchange interaction of TMD-ML. **b** [**c**] The **Q**-dependent dipoles of finite momentum longitudinal [transverse] exciton states in the upper [lower] band, whose orientations are always parallel [perpendicular] to **Q** as shown by the red [black] arrows.

lying band structure of spin-allowed valley exciton split by the *e-h* exchange interaction into a weakly parabolic lower band and a linear upper band. The exchange-induced valley-mixing of exciton leads to the unusual linear energy dispersions of exciton, which, as shown later, directly impacts the generic light-matter interactions of TMD-ML's, including that for the exciton-mediated energy transfer.

Based on the quasi-particle band structure, an exciton state of TMD-ML in the exciton band S with the center-of-mass (CoM) momentum $\hbar\mathbf{Q}$ can be written as the superposition of numerous *e-h* configurations with the momentum $\hbar\mathbf{Q}$, which reads

$$\left|\psi^{\mathrm{X}}_{S,\mathbf{Q}}\right\rangle = \frac{1}{\sqrt{\Omega_A}}\sum_{vc\mathbf{k}} A^{vc}_{S,\mathbf{Q}}(\mathbf{k})\hat{c}^{\dagger}_{c,\mathbf{k}+\mathbf{Q}}\hat{h}^{\dagger}_{v,-\mathbf{k}}|GS\rangle, \tag{1}$$

where $\hat{c}^{\dagger}_{c,\mathbf{k}+\mathbf{Q}}$ ($\hat{c}_{c,\mathbf{k}+\mathbf{Q}}$) and $\hat{h}^{\dagger}_{v,-\mathbf{k}}$ ($\hat{h}_{v,-\mathbf{k}}$) are the creation (annihilation) operators of electron of energy $\epsilon_{c,\mathbf{k}+\mathbf{Q}}$ in conduction band c carrying quasi-particle wave vector $\mathbf{k}+\mathbf{Q}$ and hole of energy $-\epsilon_{v,\mathbf{k}}$ in valence band v carrying quasi-particle wave vector $-\mathbf{k}$ for TMD-ML, respectively, $|GS\rangle$ denotes the ground state, $A^{vc}_{S,\mathbf{Q}}(\mathbf{k})$ is the amplitude of the *e-h* configuration $\hat{c}^{\dagger}_{c,\mathbf{k}+\mathbf{Q}}\hat{h}^{\dagger}_{v,-\mathbf{k}}|GS\rangle$, and Ω_A is the total area of the TMD-ML sample.

Numerically, the eigen energy, $E^{\mathrm{X}}_{S,\mathbf{Q}}$, of an exciton state $|\psi^{\mathrm{X}}_{S,\mathbf{Q}}\rangle$ can be calculated by solving the Bethe-Salpeter equation (BSE)[69,76,82,93–96], which reads

$$\left[\epsilon_{c,\mathbf{k}+\mathbf{Q}} - \epsilon_{v,\mathbf{k}}\right]A^{vc}_{S,\mathbf{Q}}(\mathbf{k}) + \sum_{v'c'\mathbf{k}'} U(vc\mathbf{k}, v'c'\mathbf{k}';\mathbf{Q})A^{v'c'}_{S,\mathbf{Q}}(\mathbf{k}') = E^{\mathrm{X}}_{S,\mathbf{Q}}A^{vc}_{S,\mathbf{Q}}(\mathbf{k}), \tag{2}$$

where the kernel of *e-h* Coulomb interaction $U(vc\mathbf{k}, v'c'\mathbf{k}';\mathbf{Q}) = -V^{d}(vc\mathbf{k}, v'c'\mathbf{k}';\mathbf{Q}) + V^{x}(vc\mathbf{k}, v'c'\mathbf{k}';\mathbf{Q})$ consists of the screened *e-h* direct Coulomb interaction $V^{d}(vc\mathbf{k}, v'c'\mathbf{k}';\mathbf{Q})$ and the *e-h* exchange Coulomb interaction $V^{x}(vc\mathbf{k}, v'c'\mathbf{k}';\mathbf{Q})$ (See Supplementary Note II for more details). Throughout this work, we consider a MoS_2-ML sandwiched by a hBN capping layer and hBN substrate, whose non-local dielectric function is evaluated by solving Poisson's equation using the approaches of refs. [97–101]. Computationally, we take the efficient methodology developed by ref. [69] that establishes and solves the density-functional-theory (DFT)-based BSE on the basis of maximally localized Wannier functions (MLWF's).

The exciton fine structures of TMD-ML's calculated by using the methodology are in excellent quantitative agreement with existing experimental results[65,67–69,74,102,103]. From the solved exciton eigen states, the transition dipole moment of a bright exciton (BX) is evaluated by $\mathbf{D}^{\mathrm{X}}_{S,\mathbf{Q}} = \frac{1}{\sqrt{\Omega_A}}\sum_{vc\mathbf{k}} A^{vc}_{S,\mathbf{Q}}(\mathbf{k})\mathbf{d}_{v,\mathbf{k};c,\mathbf{k}}$ where $\mathbf{d}_{v,\mathbf{k};c,\mathbf{k}} \equiv e\langle\psi_{v,\mathbf{k}}|\mathbf{r}|\psi_{c,\mathbf{k}}\rangle$ is the dipole moment of single-electron transition. Figure 2b [c] shows the **Q**-dependent dipole moment of the upper-band [lower-band] BX states over the momentum space. Note that the exciton dipole of light-like (particle-like) band $\mathbf{D}^{\mathrm{X}}_{+(-),\mathbf{Q}}$ is longitudinal (transverse) with respect to wave vector **Q**.

Numerically, the lowest bright exciton band structures of an hBN-sandwiched MoS_2-ML are calculated by solving the DFT-based BSE and shown in Fig. 2a. Due to the *e-h* exchange interaction, the exciton states with the opposite valleys (locked to spin) are intermixed, and the BX bands are split into a parabolic (very weakly dispersive) lower band and a quasi-linear upper one.

Besides the numerically BSE-calculated exciton band structures, we adopt the solvable pseudo-spin model for better transparent analysis. Taking the pseudo-spin model of exciton[69,75,76,92], the lower band of the lowest valley-mixed BX of a TMD-ML can be

described as $E^{X}_{S=-,\mathbf{Q}} = E^{X}_{\mathbf{0}} + \frac{\hbar^2 Q^2}{2M^X}$ and the upper linear band is

$$E^{X}_{S=+,\mathbf{Q}} = E^{X}_{\mathbf{0}} + \frac{\hbar^2 Q^2}{2M^X} + 2\gamma Q \approx E^{X}_{\mathbf{0}} + 2\gamma Q, \tag{3}$$

where $E^{X}_{\mathbf{0}}$ measures the band-edge energy of the exciton bands, γ measures half of the slope of the linear upper band and $M^X \equiv m_c + m_v = 0.85m_0$ is the total mass of exciton determined by the DFT computation. Following the study of ref. [69] and taking the 2D hydrogen model[104] that explicitly gives the exchange-free exciton wave functions in the momentum space, $A^{vc(0)}_{S,\mathbf{Q}}(\mathbf{k})$[104,105], where the superscript (0) stands for the exchange-free nature, one can show $\gamma = (4\varepsilon_0)^{-1}\left(D^X_0/\sqrt{\Omega_A}\right)^2 \propto (a_B)^{-2}$, where $D^X_0 \equiv |\mathbf{D}^X_{K/K',\mathbf{Q}}| = \sqrt{\frac{8}{\pi}}\frac{\sqrt{\Omega_A}}{a_B}d_0$, $d_0 \equiv |\mathbf{d}_{v,\mathbf{K};c,\mathbf{K}}|$[92], and $a_B \equiv (4\pi\varepsilon_0/e^2)\cdot(\hbar^2\varepsilon_{TMD}/\mu^X) = 1.93$ nm is the Bohr radius of BX for MoS_2-ML, where $\mu^X \equiv (m_c^{-1} + m_v^{-1})^{-1} = 0.21m_0$ is the reduced mass of exciton, $\varepsilon_{TMD} = \varepsilon_{MoS_2} = 7.7$ is the effective dielectric constant of MoS_2-ML. Fitting to the BSE-calculated exciton dispersion, $\gamma = 72$ meV · nm is determined in consistency with the exciton band splitting reported by refs. [75,106]. Accordingly, the transition dipole moment of exciton for MoS_2-ML is estimated to be $D^X_0/\sqrt{\Omega_A} = 0.126$(e) and the magnitude of the dipole moment of single particle transition is also estimated to be $d_0 = 0.153$(e · nm). With the small a_B, the value of γ for the tightly bound BX of TMD-ML is so large that Equation (3), $E^X_{+,\mathbf{Q}} \approx E^X_{\mathbf{0}} + 2\gamma Q$. The density of states (DOS) per unit area of exciton band is defined by $\rho_S(E) \equiv \frac{1}{\Omega_A}\sum_{\mathbf{Q}}\delta(E^X_{S,\mathbf{Q}} - E)$[107]. For the model-predicted linear upper exciton band, $\rho_{S=+}(E) = \frac{1}{8\pi\gamma^2}\left(E - E^X_{\mathbf{0}}\right)\theta\left(E - E^X_{\mathbf{0}}\right)$ where $\theta(E)$ is the step function, increases linearly with increasing E, as shown by Fig. 4c. For the BSE-calculated upper exciton band following a sub-linear dispersion, the DOS of exciton is generally higher than that simulated by the pseudo-spin model of exciton, as shown by Fig. 4c.

Exciton-mediated energy transfer from QD's to TMD-ML's

According to Fermi's golden rule, the rate of the FRET from a QD with the excitation energy, ε^X_0, to a TMD-ML is evaluated by

$$\Gamma_{DA}\left(\varepsilon^X_0, d\right) = \frac{2\pi}{\hbar}\sum_{S\mathbf{Q}}\left|\widetilde{M}_{S,\mathbf{Q}}\right|^2\delta\left(E^X_{S,\mathbf{Q}} - \varepsilon^X_0\right), \tag{4}$$

where the delta function ensures the energy conservation and the matrix element of the Förster coupling from the lowest exciton of QD reads

$$\widetilde{M}_{S,\mathbf{Q}} = \int d^3\mathbf{r}\int d^3\mathbf{r}' eP^{X*}_{S,\mathbf{Q}}(\mathbf{r})\frac{1}{4\pi\varepsilon_0\varepsilon_b|\mathbf{r} - \mathbf{r}' - \mathbf{O}'|}eP^X_0(\mathbf{r}'), \tag{5}$$

where $\mathbf{O}' = (0, 0, d)$ is the central position of QD measured from the origin point, $\mathbf{O} = (0, 0, 0)$, in the plane of TMD-ML, $P^X_0(\mathbf{r}) \approx \phi^{v*}_0(\mathbf{r})\phi^c_0(\mathbf{r})$ is the pair-density of the lowest exciton state of QD, $\phi^{c/v}_0(\mathbf{r})$ is the wave function of the lowest electron/hole state of the QD, $P^X_{S,\mathbf{Q}}(\mathbf{r}) \equiv \frac{1}{\sqrt{\Omega_A}}\sum_{vc\mathbf{k}}A^{vc}_{S,\mathbf{Q}}(\mathbf{k})\psi^*_{v,\mathbf{k}}(\mathbf{r})\psi_{c,\mathbf{k}+\mathbf{Q}}(\mathbf{r})$ is the pair-density of exciton transition in the TMD-ML, and ε_b is the effective dielectric constant of dielectric environment.

Here, we neglect the weak Coulomb correlation for strongly confining QD's and consider the exciton wave function of QD as the direct product of $\phi^{v*}_0(\mathbf{r})$ and $\phi^c_0(\mathbf{r})$. Taking the electrical dipole approximation (See Supplementary Note III for derivation details), we can show that

$$\widetilde{M}_{S,\mathbf{Q}} = -\frac{1}{\Omega_A}\mathbf{D}^{X*}_{S,\mathbf{Q}}\cdot\boldsymbol{\varepsilon}_{\mathbf{Q}}, \tag{6}$$

where

$$\boldsymbol{\varepsilon}_{\mathbf{Q}} = \frac{-i}{2\varepsilon_0\varepsilon_b}e^{-Qd}\mathbf{Q}(-i\hat{\mathbf{Q}} - \hat{\mathbf{z}})\cdot\mathbf{D}^X_{QD} \tag{7}$$

Table 1. Parameters used in the model simulations of this work.

Parameter (unit)	Value	References	Parameter (unit)	Value	Reference
$m_c(m_0)$	0.39	Refs. [122–126]	$D^X_{QD}(e\cdot nm)$	0.44	Refs. [127–129]*
$m_v(m_0)$	0.46	Refs. [122–126]	$d_0(e\cdot nm)$	0.153	Refs. [69,130]
ε_{MoS_2}	7.7	Ref. [69]***	$E^X_{\mathbf{0}}$(eV)	1.9	Refs. [41,52]
ε_{hBN}	4	Refs. [131–133]	γ(meV · nm)	72	Refs. [75,106]**

*The transition dipole moment of exciton, $D^X_{QD} = 0.44e\cdot nm$, for CdSe QDs is estimated according to the formalisms of refs. [122–124].
**The parameter of γ is determined by fitting Equation (3) to the BSE-calculated upper exciton band in the momentum range from $0q_c$ to $10q_c$, which is consistent with the exciton band splitting reported by refs. [75,106].
***With the DFT-calculated effective masses and following the study of ref. [69], we adopt the dielectric constant $\varepsilon_{MoS_2} = 7.7$.

is the **Q**-component of the Förster field induced by the dipole moment of the QD, $\mathbf{D}^X_{QD} \equiv \langle\phi^v_0|e\mathbf{r}|\phi^c_0\rangle$. Throughout this work, we consider hBN as the spacer material between CdSe QDs with $|\mathbf{D}^X_{QD}| = 0.44\,e\cdot nm$ and a MoS_2-ML and take $\varepsilon_b = \varepsilon_{hBN} = 4$ (See Table 1).

From Equation (7), one can realize that the **Q**-dependence of the strength of a Förster field is governed by two competing factors: (1) the linear Q term and (2) the exponential decay e^{-Qd}. The linear **Q**-dependent factor (1) originates from the fact that the strength of the dipole-dipole interaction between a point-dipole (QD) and dipoles periodically distributed over a 2D plane (TMD-ML) increases with increasing the periodicity of the in-plane distributed dipoles, i.e., increasing Q. As increasing Q, the planar density of dipoles increases, and the total FRET rate is enhanced. On the other hand, the exponential decay factor is associated with the near-field nature of the Förster field, which contains the evanescent mode decaying exponentially along the z direction ($\propto e^{-\kappa d}$), characterized by an imaginary wave vector, $k_z = i\kappa$. Since the magnitude of the wave vector of a radiation, $k = \sqrt{k_x^2 + k_y^2 + k_z^2}$, should remain invariant to fulfill the momentum conservation law, the imaginary wave vector carried by the evanescent mode allows the momentum of the in-plane components of a Förster field exceeds the light-cone edge, i.e., $\sqrt{k_x^2 + k_y^2} > q_c$, and enables the Förster field to couple MFDX's. As a result of the two competing factors, the magnitude of the matrix element of Förster coupling, $\widetilde{M}_{S,\mathbf{Q}}$, shows a maximum peak at

$$Q = 1/d \equiv Q_0. \tag{8}$$

Without losing the generality, we consider $\mathbf{D}^X_{QD} = D^X_{QD}\hat{\mathbf{x}}$ for elongated CdSe QD's throughout this work. Figure 3a presents the numerically calculated vectorial **Q**-components of the Förster field, $\boldsymbol{\varepsilon}_{\mathbf{Q}}$, over the **Q**-space. As expected, one sees that the maximal **Q**-components of the Förster field are indeed located at $Q_0 = 1/d$, far away from the light cone of BX. Because of the longitudinal nature of the dipole-induced Förster field, the orientation of $\boldsymbol{\varepsilon}_{\mathbf{Q}}$ remains parallel to the direction of **Q**. Hence, according to Eqs. (6) and (7), a Förster field directly couples the longitudinal exciton states with $\mathbf{D}^X_{+,\mathbf{Q}}\|\boldsymbol{\varepsilon}_{\mathbf{Q}}$ but not the transverse exciton states of the lower band with $\mathbf{D}^X_{-,\mathbf{Q}} \perp \boldsymbol{\varepsilon}_{\mathbf{Q}}$.

Figure 3c shows the square of the matrix element of the Förster coupling for the longitudinal exciton of MoS_2-ML, $|\widetilde{M}_{+,\mathbf{Q}}|^2$, induced by the QD apart by $d = 8$ nm. Since $d \ll \lambda \sim 10^2$–10^3 nm, the optimally coupled exciton states with $Q_0 = 1/d \approx 13q_c$ for $d = 8$ nm are far away from the small reciprocal area of light-cone and belong to the MFDX states.

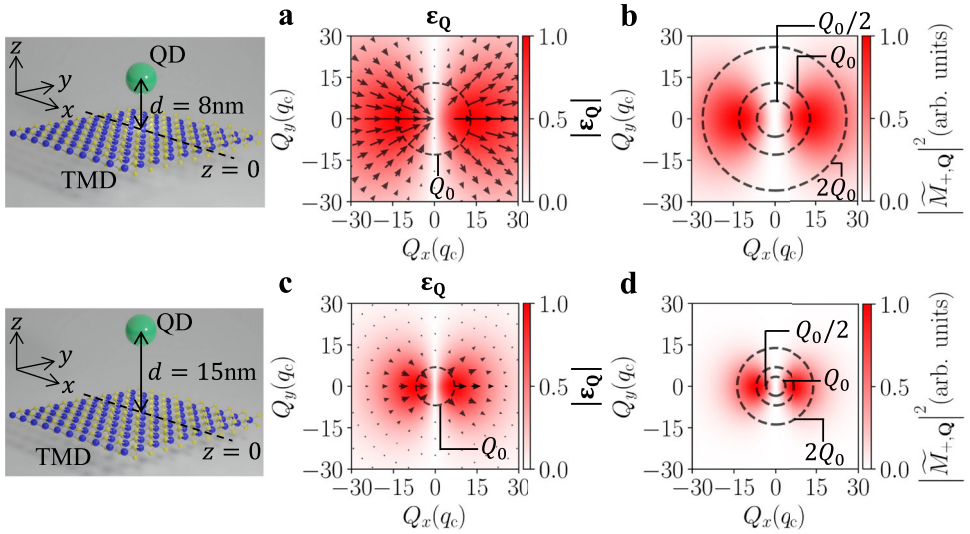

Fig. 3 Förster field, $\varepsilon_{\mathbf{Q}}$, and square of the Q-dependent matrix element of Förster coupling $|\widetilde{M}_{+,\mathbf{Q}}|^2$. **a** The contour plot (arrows) represents the intensity (direction and magnitude) of amplitude, $\boldsymbol{\varepsilon}_{\mathbf{Q}}$, of the longitudinal plane-wave components at $z = 0$ with the wave vector **Q** in the Förster field. Note that the plotted values have been normalized by their greatest value in the plotted **Q**-plane. **b** The square of the **Q**-dependent matrix element of Förster coupling, which is determined by (**b**) according to Equation (6). Note that the Förster coupling is maximum at $\mathbf{Q}_0 = (Q_0, 0)$ where $Q_0 = 1/d \approx 13q_c$ and still remains significantly high in the regime around $\mathbf{Q}_0$ where the magnitudes of the wave vectors are in the range between $0.5Q_0$ and $2Q_0$. **c**, **d** Simulated results for the same QD and MoS_2-ML but with the longer QD-TMD distance $d = 15$ nm. One sees that, with the longer d, the MFDX states under the significant Förster coupling possess the smaller $Q_0 \approx 7q_c$.

Figure 3c, d shows the calculated results of the TMD-QD system with the longer $d = 15$ nm. The longer d makes the smaller wave vectors of $Q_0 \approx 7q_c$ where the Förster couplings are maximal. Hence, the regime of optimal Förster coupling over the **Q** plane in Fig. 3d is shrunk, and less MFDX states are essentially involved in the FRET for the QD-TMD system with longer d.

Excitation-energy dependence of dark-exciton-dictated FRET

Substituting the $\widetilde{M}_{S,\mathbf{Q}}$ of Equation (6) into Equation (4) and taking into account all the coupled longitudinal exciton states, one can formulate the total rate of FRET as a function of excitation energy, $\varepsilon_0^{\mathrm{X}}$, as

$$\Gamma_{DA}(\varepsilon_0^{\mathrm{X}}, d) = \frac{2\pi}{\hbar}\bar{\xi}_+(\varepsilon_0^{\mathrm{X}}, d)\rho_+(\varepsilon_0^{\mathrm{X}}), \tag{9}$$

where the averaged Förster coupling for the exciton states with the energy $E^{\mathrm{X}}_{+,\mathbf{Q}} = \varepsilon_0^{\mathrm{X}}$ is defined by and derived as

$$\bar{\xi}_+(\varepsilon_0^{\mathrm{X}}, d) \equiv \frac{\sum_{\mathbf{Q}}\left|\widetilde{M}_{+,\mathbf{Q}}\right|^2\delta\left(E^{\mathrm{X}}_{+,\mathbf{Q}} - \varepsilon_0^{\mathrm{X}}\right)}{\frac{1}{\Omega_A}\sum_{\mathbf{Q}}\delta\left(E^{\mathrm{X}}_{+,\mathbf{Q}} - \varepsilon_0^{\mathrm{X}}\right)} = \frac{\left[D^{\mathrm{X}}_{QD}\right]^2\left[D^{\mathrm{X}}_{0}\right]^2}{8\varepsilon_0^2\varepsilon_b^2\Omega_A}Q_R^2 e^{-2Q_R d}, \tag{10}$$

where

$$Q_R \equiv (\varepsilon_0^{\mathrm{X}} - E^{\mathrm{X}}_{\mathbf{0}})/2\gamma \tag{11}$$

is the magnitude of the wave vectors of the resonant exciton states to the excitation energy of the QD. Note that the maximum Förster coupling critically occurs as $Q_R = Q_0$, leading to

$$\Delta\varepsilon_0^{\mathrm{X}} = E^{\mathrm{X}}_{+,Q_0} - E^{\mathrm{X}}_{\mathbf{0}} = 2\gamma/d, \tag{12}$$

where $\Delta\varepsilon_0^{\mathrm{X}} \equiv \varepsilon_0^{\mathrm{X}} - E^{\mathrm{X}}_{\mathbf{0}}$ measures the energy difference between the excitation energy of QD and the lowest exciton energy, $E^{\mathrm{X}}_{\mathbf{0}}$. This indicates that the size of QD that determines $\varepsilon_0^{\mathrm{X}}$ and the distance between QD and TMD-ML, d, act as two tuning knobs related by γ for optimizing the energy transfer rate. For tightly bound exciton with $a_B \sim 1$–2 nm in a MoS_2-ML, the value of $\gamma = \frac{2d_0^2}{\pi\varepsilon_0}(a_B)^{-2} \approx 100$ meV · nm is significantly large, and to achieve the maximal FRET, the excitation energy of QD should be properly higher than the BX states to match the energy of the longitudinal exciton states with $Q = Q_0$. In Fig. 2a, we see that $\Delta E^{\mathrm{X}}_{Q_0,\mathbf{0}} \equiv E^{\mathrm{X}}_{+,Q_0} - E^{\mathrm{X}}_{\mathbf{0}} \approx 18$meV (≈16 meV) for the QD-TMD system with $d = 8$ nm according to the model-predicted (BSE-calculated) exciton band structure of MoS_2-ML. One also finds in Fig. 3b that $|\widetilde{M}_{+,Q}|$ persists high for the finite momentum exciton states over a wide **Q**-regime where $Q \in \{Q_0/2, 2Q_0\}$, corresponding to the energy range, $\Delta E^{\mathrm{X}}_{2Q_0,Q_0/2} \equiv E^{\mathrm{X}}_{+,2Q_0} - E^{\mathrm{X}}_{+,Q_0/2} = 27\,\mathrm{meV}(17\,\mathrm{meV})$, according to the model-predicted (BSE-calculated) upper exciton band. This indicates, due to the large γ of TMD-ML, the robustness of efficient FRET's from QD's to TMD-ML's against the variation of the excitation energies of QD's over a wide range of $\Delta E^{\mathrm{X}}_{2Q_0,Q_0/2}$.

By contrast, in mesoscopic quasi-2D systems, e.g., epitaxial semiconductor quantum wells, excitons are weakly bound and possess the larger Bohr radius $a_B \sim 10$ nm[108], leading to much smaller $\gamma \sim$ few meV · nm[109]. With the nearly vanishing γ (leading to small $\Delta\varepsilon_0^{\mathrm{X}}$), both BX bands of a quantum well remain weakly dispersive, and the excitation energies of QD's must be critically little higher than that of BX to maximize the FRET rate, i.e., $\Delta\varepsilon_0^{\mathrm{X}} \gtrsim 0$.

Figure 4a shows the calculated total FRET rates, $\Gamma_{DA}(\varepsilon_0^{\mathrm{X}}, d)$ as a function of the excitation energy of QD-donor, of the exciton-mediated FRET to a MoS_2-ML acceptor apart from the QD by $d = 8$ nm with the full counting of the MFDX exciton states of the longitudinal exciton band calculated by numerically solving DFT-based BSE (blue solid curve) and by taking the pseudo-spin model (red dashed curve).

The simulated rate of $\Gamma_{DA}(\varepsilon_0^{\mathrm{X}}, d)$ based on the BSE-calculated exciton band structure is shown faster but remains significant over a slightly small energy range of $\varepsilon_0^{\mathrm{X}}$ than the pseudo-spin model of exciton because the slightly sub-linear dispersion of the BSE-calculated longitudinal upper band leads to the higher DOS (See Fig. 4c) and smaller energy range of $\Delta E^{\mathrm{X}}_{2Q_0,Q_0/2}$ where the Förster coupling is significant. Remarkably, the excitation energies of QD's falling in the tens-of-meV scaled range of $\Delta E^{\mathrm{X}}_{2Q_0,Q_0/2}$ covers only the lowest 1s exciton bands and access neither the higher Rydberg exciton states nor the *e-h* continuum states, which are above the 1s exciton states by hundreds of meV[82,95]. Thus, TMD-ML's

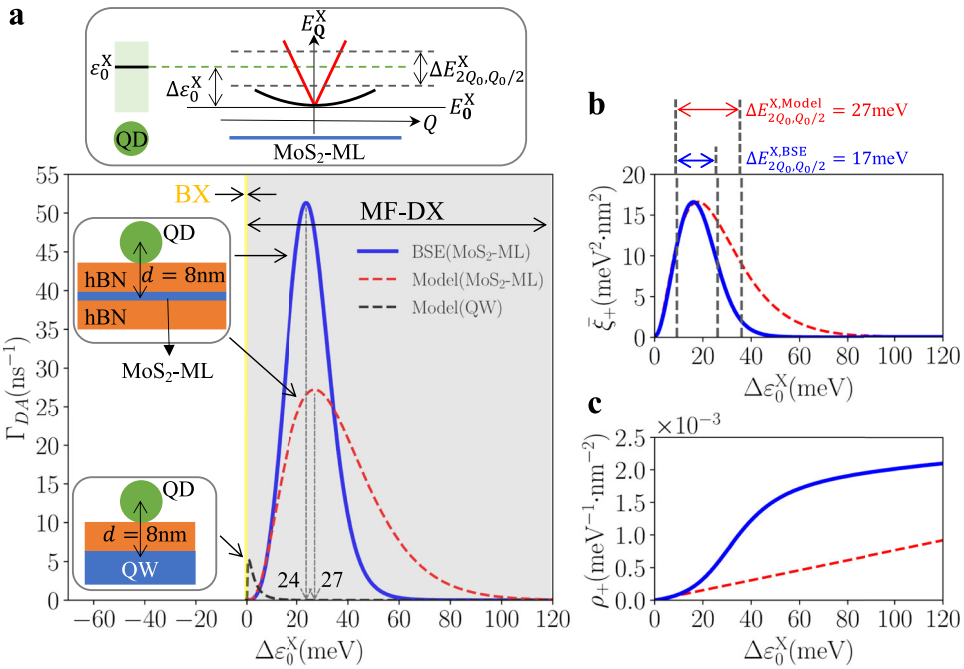

Fig. 4 Rate of exciton-mediated FRET between a QD and a MoS_2, averaged Förster coupling for all resonantly coupled exciton states, $\bar{\xi}_+(\Delta\varepsilon_0^X)$, and density of state (DOS) of exciton upper band $\rho_+(\Delta\varepsilon_0^X)$. a Blue (red dashed) curve: The BSE-calculated (model-predicted) rate of exciton-mediated FRET between a QD and a MoS_2-ML with $d = 8$ nm, as a function of $\Delta\varepsilon_0^X \equiv \varepsilon_0^X - E_0^X$. One notes that the rates of the FRET of the TMD-ML remain significantly high over a wide range of excitation energy, from tens of meV to over 60 meV, in the regime of MFDX. Black dashed curve: The model-predicted rate of exciton-mediated FRET between a QD and a mesoscopic quantum well with the same $d = 8$ nm, where exciton in the quantum well is weakly bound with negligible *e-h* exchange interaction. **b** Blue (red dashed curve) curve: The BSE-calculated (model-predicted) averaged Förster coupling for all resonantly coupled exciton states, $\bar{\xi}_+$, as a function of $\Delta\varepsilon_0^X$. The maximum Förster coupling occurs as $Q_0 = 1/d$, corresponding to the BSE-calculated (model-predicted) energy of the exciton states, $\Delta E^X_{2Q_0,Q_0/2} \equiv E^X_{+,2Q_0} - E^X_{+,Q_0/2} = 17$ meV(27 meV). **c** Blue (red dashed) curve: The BSE-calculated (model-predicted) density of states (DOS) of exciton upper band $\rho_+(\Delta\varepsilon_0^X)$.

exceptionally serve as an excellent acceptor system for the FRET mediated purely by excitons.

To highlight the pronounced excitonic effects of TMD-ML on FRET, we calculate the rate of the FRET from the same QD to a mesoscopic quantum well where the 2D excitons are loosely bound, with a large Bohr radius, typically $a_B = 10$ nm (See the black dashed curve in Fig. 4a). The large Bohr radius of weakly bound exciton suppresses the *e-h* exchange interaction and retains the degenerate weakly dispersive exciton bands. As one sees in Fig. 4a, the rate of FRET between the QD and the quantum well with the same distance $d = 8$ nm is much lower than that of TMD-ML because of the small dipole moment of weakly bound exciton in a quantum well (QW). With the weak dispersion of the parabolic exciton bands, the rate of FRET to a QW from a photo-excited QD is significant only as the excitation energy of QD critically falls in the narrow energy range, $\Delta\varepsilon_0^X \sim 0 - 10$ meV, slightly above the exciton band edge of QW (See the black curve in Fig. 4a). Once the excitation energy of QD is out of the narrow energy range ($\Delta\varepsilon_0^X > 10$meV), the FRET rate from a QD to a mesoscopic QW drops to almost vanishing.

Distance-dependence of dark-exciton-dictated FRET

From Equation (10), it is shown that the calculated rate of the *exciton*-mediated FRET from a QD to a TMD-ML by the quantum theory yields an exponential dependence on the QD-TMD distance, $\Gamma_{DA} \propto e^{-2Q_R d}$, rather than the d^{-4}-power-law ($\Gamma_{DA} \propto d^{-4}$) as predicted by the classical FRET model for 0D-2D systems[17,37,60,110–115]. This is because, in the quantum regime, the CoM motion of an exciton in a 2D system is described by a spatially extended plane-wave function instead of a localized point dipole as considered in the classical model[113,116]. Practically, the wave aspect of exciton in the ideal quantum regime might be suppressed by introducing a variation of exciton momentum to the 2D exciton system. This situation occurs, e.g., in the FRET from an inhomogeneous QD layer where the unequal QD's with various excitation energies simultaneously couple the different exciton states of TMD-ML with various CoM momenta. To confirm the scenario, we consider an inhomogeneous QD-layer where the excitation energies of QD's are considered to follow a Gaussian distribution over energy, $f(\varepsilon_0^X; \bar{\varepsilon}_0^X, \sigma_\varepsilon) = \left(1/\sqrt{2\pi\sigma_\varepsilon^2}\right) \exp\left(-\left(\varepsilon_0^X - \bar{\varepsilon}_0^X\right)^2 / 2\sigma_\varepsilon^2\right)$, where $\bar{\varepsilon}_0^X$ is the average excitation of QD-ensemble and σ_ε is the parameter of energy deviation defined by $\sigma_\varepsilon^2 = \overline{\left(\varepsilon_0^X - \bar{\varepsilon}_0^X\right)^2}$. For simplicity, we consider that each QD's in the ensemble have the same distance to the TMD-ML and neglect the energy transfer between QD's. Accordingly, the average rate of energy transfer from a photo-excited inhomogeneous QD-layer to a TMD-ML is defined as,

$$\bar{\Gamma}_{DA}(\bar{\varepsilon}_0^X, \sigma_\varepsilon, d) \equiv \int d\varepsilon_0^X \Gamma_{DA}(\varepsilon_0^X, d) f(\varepsilon_0^X; \bar{\varepsilon}_0^X, \sigma_\varepsilon). \tag{13}$$

First, let us consider the *homogeneous* QD-layer where $f(\varepsilon_0^X; \bar{\varepsilon}_0^X, \sigma_\varepsilon \to 0) = \delta(\varepsilon_0^X - \bar{\varepsilon}_0^X)$. Taking $\bar{\varepsilon}_0^X - E_0^X = 45$meV, the linear and log plots of the normalized rate, $\bar{\Gamma}_{DA}(d)/\bar{\Gamma}_{DA}(5\text{nm})$, from the *homogeneous* QD-layer to a MoS_2-ML with varying $d = 5$ nm to 20 nm are shown by the red dashed curves in Fig. 5b, c, respectively. As inferred from Equation (9), the calculated rate of FRET from the *homogeneous* QD-layer, similar to a single QD, does show an exponential decay with increasing d, i.e., $\bar{\Gamma}_{DA} \propto e^{-2Q_R d}$ [60–62,64], where Q_R is the wave vector of the resonantly coupled exciton states and

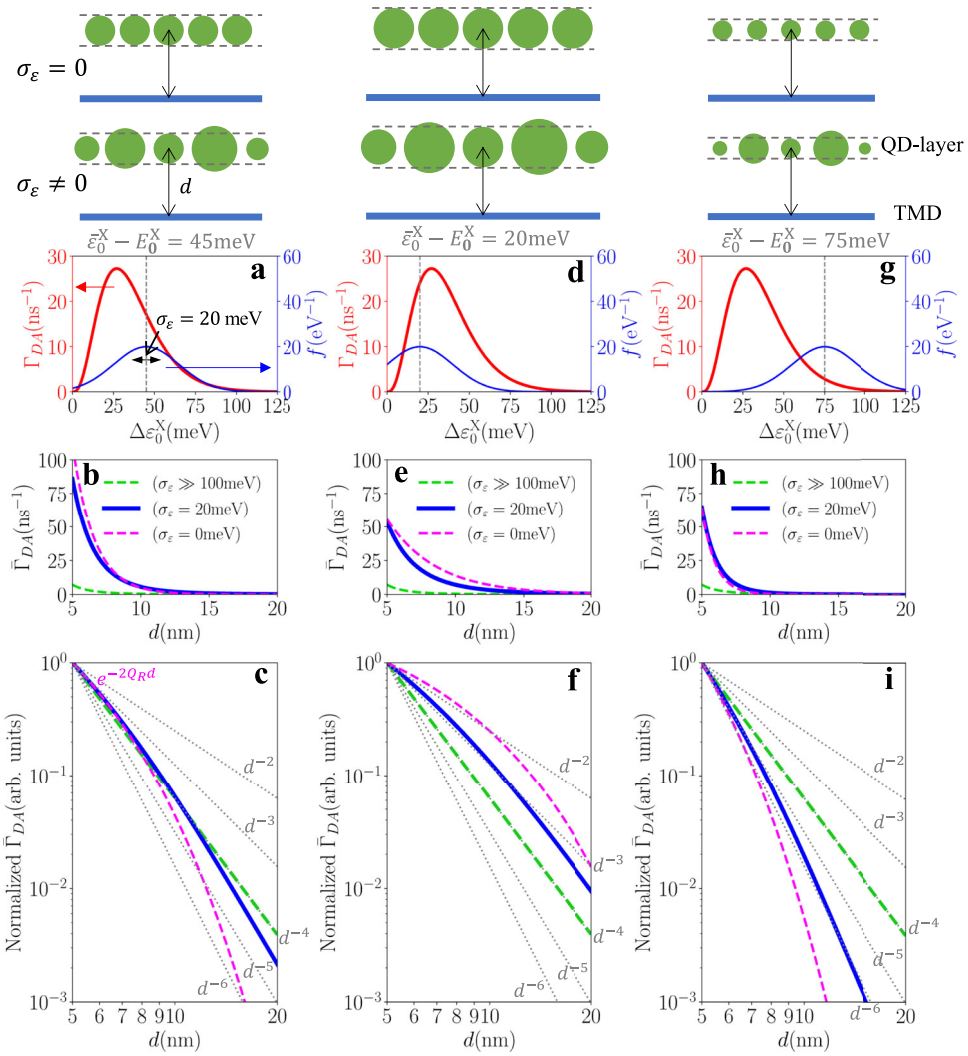

Fig. 5 Distance dependence of the FRET to a MoS_2-ML from an inhomogeneous QD-layer whose excitation energy distribution is modeled by the Gaussian function parametrized by the average excitation energy, $\bar{\varepsilon}_0^X$, and energy variation, σ_ε. **a** Red curve: the rate of FRET between a QD and a MoS_2-ML with $d = 8$ nm, as a function of excitation energy of QD. Blue curve: the Gaussian distribution of excitation energy for an inhomogeneous QD-layer with the average energy coincident with the energy of the maximum FRET rate, $\bar{\varepsilon}_0^X - E_0^X = 45$ meV, and the energy variation, $\sigma_\varepsilon = 20$ meV. **b** [**c**] Blue curves: The linear [logarithm] plot of the QD-TMD distance dependence of the rate of the FRET between a MoS_2-ML and an inhomogeneous QD-layer with $\sigma_\varepsilon = 20$ meV. For comparison, the distance dependences of the FRET for the same QD-TMD system but with $\sigma_\varepsilon = 0$ meV and $\sigma_\varepsilon \gg 100$ meV are presented by the magenta and green dashed lines, respectively. **d**–**f** consider the FRET between a TMD-ML and a QD-layer system with the lower average excitation energy, $\bar{\varepsilon}_0^X - E_0^X = 20$ meV. **g**–**i** consider the FRET between a TMD-ML and a QD-layer system with the higher average excitation energy, $\bar{\varepsilon}_0^X - E_0^X = 75$ meV.

does not follow the classically predicted d^{-4} distance dependence, i.e., $\Gamma_{DA} \propto d^{-4}$ [17,37,60,110–115].

Next, we consider *inhomogeneous* QD-layers with finite energy variations, $\sigma_\varepsilon \neq 0$. We shall show that the interplay between the energy variation of an inhomogeneous QD-layer, σ_ε, and the exchange-induced valley splitting of the exciton bands of a TMD-ML, γ, leads to the unusual d-dependence of the FRET between the 0D- and 2D-systems. For more analysis, we expand the average rate of energy transfer expressed by Equation (13) as a function of σ_ε and d in the asymptotic series,

$$\bar{\Gamma}_{DA}(\bar{\varepsilon}_0^X, \sigma_\varepsilon, d) = \frac{\alpha}{d^4}\left[1 + 4\left(\frac{\gamma}{\sigma_\varepsilon d}\right)\Delta + 10\left(\frac{\gamma}{\sigma_\varepsilon d}\right)^2(\Delta^2 - 1) + \cdots\right], \tag{14}$$

where $\alpha = (3[D_{QD}^X]^2[D_0^X]^2/64\sqrt{2\pi}\hbar\varepsilon_0^2\varepsilon_b^2\Omega_A\sigma_\varepsilon)\exp(-\Delta^2/2)$ and $\Delta \equiv (\bar{\varepsilon}_0^X - E_0^X)/\sigma_\varepsilon$ measures the energy difference between the average excitation energy of the QD donors and the lowest exciton energy of the TMD-ML acceptors scaled by the inhomogeneity-induced energy variation of QD donors.

In the limits of long donor-acceptor distance or large inhomogeneity, i.e., $d \gg \gamma/\sigma_\varepsilon$, Equation (14) shows that the FRET rate approaches the classically predicted d^{-4}-dependence[17,37,60,110–115]. Contrarily, as the donor-acceptor distance is very short or the QD-donors are very homogeneous, i.e., $d \ll \gamma/\sigma_\varepsilon$, all high-order terms in the asymptotic series (14) are non-negligible, and their summation restores the exponential distance dependence of the FRET in the quantum regime ($\bar{\Gamma}_{DA} \propto e^{-2Q_R d}$)[60–62,64].

In between the two extreme situations, i.e., $d \sim \gamma/\sigma_\varepsilon$, a few higher order terms (d^{-5}, d^{-6}, ...) next to the d^{-4}-term might emerge to dictate the distance dependence of the FRET under appropriate conditions of Δ. Remarkably, due to the enhanced *e-h* exchange interaction, the value of γ for atomically thin TMD-ML's is three orders of magnitude greater than that of bulk. With the large value of $\gamma \sim 10^2$ meV · nm of a TMD-ML and the typical energy variation of a QD-layer $\sigma_\varepsilon \sim 10^1$–$10^2$ meV, the critical d that

distinguishes the classical and quantum regimes falls in the range of $d \sim 1$–10 nm, which is the typical distance between QD donors and TMD-ML acceptors in reality. Therefore, the *e-h* exchange interaction of MFDX's plays a key role in the distance-dependent FRET between QD donors and TMD-ML acceptors, and under certain conditions, might result in the unusual distance dependence deviating from the d^{-4} or the exponential distance dependences predicted in the classical and quantum regimes, respectively.

As a model test, we first set an extremely large energy variation, $\sigma_\varepsilon \gg 100$ meV, to mimic and simulate the classical FRET. As shown by green dashed lines in Fig. 5c, f, i, we indeed retain the *d*-dependence of $\bar{\Gamma}_{DA}$ that perfectly follows the classically predicted power-law, $\bar{\Gamma}_{DA} \propto d^{-4}$ [17,37,60,110–115], for the FRET from the extremely inhomogeneous QD-layer.

For realistic simulation, one might take the moderate energy variation like $\sigma_\varepsilon = 20$ meV, with which the length scale of $\gamma/\sigma_\varepsilon = 3.6$ nm such that the distance dependence of $\bar{\Gamma}_{DA}$ shows a multi-power-law behavior, as one can see from Equation (14) and shown by blue solid curves in Fig. 5c. Carefully examining Fig. 5c, one finds that the rate of the FRET between a TMD-ML and QD's with $\sigma_\varepsilon = 20$ meV exhibits the weaker (higher) *d*-dependence than the d^{-4}-power law in the short (long) distance regime where $d < 10$ nm ($d > 10$ nm).

Figure 5d–f shows the simulated rate of the FRET to a TMD-ML from an inhomogeneous QD-layer with a lower average excitation energy, $\bar{\varepsilon}_0^X - E_{\mathbf{0}}^X = 20$meV. With the low excitation energy, the FRET of the QD-TMD system, in general, shows a much weaker *d*-dependence in Fig. 5e, f, as compared with Fig. 5b, c.

The weak *d*-dependence of the FRET from the QD-layer with the low excitation energy results from the fact that the resonantly coupled MFDX states of TMD-ML in the FRET possess the low energies and small momenta, Q_R, the latter of which leads to the weak *d*-dependence according to Equation (9). Figure 5g–i shows the simulated results of FRET between a TMD-ML and an inhomogeneous QD-layer with high average excitation energy, $\bar{\varepsilon}_0^X - E_{\mathbf{0}}^X = 75$meV. As compared with Fig. 5d–f, the simulated FRET from the QD-layer with the high excitation energy shows a fast decay with increasing distance. With the long $d > 10$ nm, the distance dependence of FRET rate follows the d^{-n} power law with $n > 5$.

From our studies, the *d*-dependence of dark-exciton-mediated FRET of a TMD-ML is realized not to certainly follow the d^{-4}-power-law as classically predicted but show a multi-exponential decay that is substantially affected by extrinsic factors such as the inhomogeneity of materials. This accounts for the often-seen ambiguity of the *d*-power-law-fitting of the measured FRET rates reported by many existing experiments[19,22,28,30,34,37,39].

In summary, we present a theoretical investigation of exciton-mediated Förster resonant energy transfers from photo-excited quantum dots to monolayer TMD's. In contrast to conventional semiconductor bulk or mesoscopic nano-materials, excitons in atomically thin TMD-MLs are tightly bound by the extraordinarily strong Coulomb interaction, leading to large transition dipole moments and unusual exchange-induced exciton band dispersions. The large dipole moment of exciton directly enhances the FRET rate of a TMD-ML to be faster than the FRET of mesoscopic quantum wells by several times. Moreover, our studies point out that the FRET of a TMD-ML is dictated by momentum-forbidden dark excitons rather than the commonly expected bright excitons. The momentum-forbidden dark exciton states of TMD-ML that follow the unusual linear exciton band dispersion are shown to substantially grade up the efficiency and robustness of FRET of TMD-ML against the inhomogeneity of donor ensembles. With the enhanced electron-hole exchange interaction of exciton in an atomically thin TMD-ML acceptors and certain energy variations of inhomogeneous QD donors, the FRET between QD's and a TMD-ML is not necessary to follow the commonly recognized d^{-4} or exponential distance power laws but could exhibit the unusual d^{-5} or even higher order distance dependence. Hence, the measured distance power-law dependences of the FRET's of TMD-ML's actually cannot reflect the dimensionality of the donor-acceptor system. Our studies reveal the essential role of momentum-forbidden dark excitons in the FRET of generic 2D materials and suggest the prospect of dark-exciton-based near-field technology using 2D materials.

METHODS

Density functional theory (DFT) calculations

In this work, we performed density functional theory (DFT) calculations using the Vienna Ab initio Simulation Package (VASP)[117] to determine the quasi-particle band structure of MoS_2 monolayers (MoS_2-ML's). First, we optimized the cell volume and atomic position with the PBE functional[118] until the atomic forces converged below 0.005 eV · Å^{-1}, yielding a lattice constant of $a_0 = 3.166$Å. To prevent artificial interactions between periodic layers, we introduced a 30 Å vacuum layer in the out-of-plane direction. Subsequently, self-consistent calculations were conducted using the HSE06 hybrid functional[119] to solve the Kohn-Sham equations, taking into account the spin-orbit coupling (SOC). The plane-wave cutoff energy for the expansion of wave functions and PAW potentials is set to be 500 eV. The first Brillouin zone is sampled by a $10 \times 10 \times 1$ Monkhorst-Pack grid. The break condition for the electronic self-consistent loop is set to be 10^{-6} eV. The calculated quasi-particle band structures of a MoS_2-ML are shown in Supplementary Fig. 1a.

Bethe-Salpeter equation (BSE) for exciton spectra

Based on the calculated quasi-particle band structure, we employed the methodology developed in ref. [69] to solve the Bethe-Salpeter equation (BSE) and determine the exciton spectra of a hBN-encapsulated MoS_2 monolayer. To reduce the computational cost associated with evaluating the electron-hole interaction kernel, we employed the Wannier90 package[120,121] to transform the quasi-particle states into maximally localized Wannier functions (MLWF's). Additionally, we determined the non-local dielectric function in the kernel of the screened electron-hole direct Coulomb interaction by solving Poisson's equation, following the approaches outlined in refs. [97–101].

DATA AVAILABILITY

The data supporting this study's findings are available from the corresponding author upon reasonable request.

CODE AVAILABILITY

The codes supporting this manuscript's findings are available from the corresponding author upon reasonable request.

Received: 2 February 2023; Accepted: 14 July 2023;
Published online: 25 July 2023

REFERENCES

1. Förster, T. Energiewanderung und fluoreszenz. *Naturwissenschaften* **33**, 166–175 (1946).
2. Förster, T. Zwischenmolekulare energiewanderung und fluoreszenz. *Ann. Phys.* **437**, 55–75 (1948).
3. Förster, T. 10th spiers memorial lecture. Transfer mechanisms of electronic excitation. *Discuss. Faraday Soc.* **27**, 7–17 (1959).
4. Medintz, I. & Hildebrandt, N. *FRET—Förster Resonance Energy Transfer*. https://onlinelibrary.wiley.com/doi/abs/10.1002/9783527656028.fmatter (Wiley, 2013).
5. Jones, G. A. & Bradshaw, D. S. Resonance energy transfer: from fundamental theory to recent applications. *Front. Phys.* **7**, 100 (2019).

6. Engel, G. S. et al. Evidence for wavelike energy transfer through quantum coherence in photosynthetic systems. *Nature* **446**, 782–786 (2007).
7. Lee, H., Cheng, Y.-C. & Fleming, G. R. Coherence dynamics in photosynthesis: protein protection of excitonic coherence. *Science* **316**, 1462–1465 (2007).
8. Cheng, Y.-C. & Fleming, G. R. Dynamics of light harvesting in photosynthesis. *Annu. Rev. Phys. Chem.* **60**, 241–262 (2009).
9. Lambert, N. et al. Quantum biology. *Nat. Phys.* **9**, 10–18 (2013).
10. Chenu, A. & Scholes, G. D. Coherence in energy transfer and photosynthesis. *Annu. Rev. Phys. Chem.* **66**, 69–96 (2015).
11. Wilkins, D. M. & Dattani, N. S. Why quantum coherence is not important in the Fenna-Matthews-Olsen complex. *J. Chem. Theory Comput.* **11**, 3411–3419 (2015).
12. Franzl, T., Klar, T. A., Schietinger, S., Rogach, A. L. & Feldmann, J. Exciton recycling in graded gap nanocrystal structures. *Nano Lett.* **4**, 1599–1603 (2004).
13. Liu, Y., Summers, M., Edder, C., Fréchet, J. & McGehee, M. Using resonance energy transfer to improve exciton harvesting in organic-inorganic hybrid photovoltaic cells. *Adv. Mater.* **17**, 2960–2964 (2005).
14. Cnops, K. et al. 8.4% efficient fullerene-free organic solar cells exploiting long-range exciton energy transfer. *Nat. Commun.* **5**, 1–6 (2014).
15. Guzelturk, B. & Demir, H. V. Near-field energy transfer using nanoemitters for optoelectronics. *Adv. Funct. Mater.* **26**, 8158–8177 (2016).
16. Zhang, Y.-N. et al. Efficient quantum-dot light-emitting diodes employing thermally activated delayed fluorescence emitters as exciton harvesters. *ACS Appl. Mater. Interfaces* **10**, 7435–7441 (2018).
17. Achermann, M. et al. Energy-transfer pumping of semiconductor nanocrystals using an epitaxial quantum well. *Nature* **429**, 642–646 (2004).
18. Achermann, M., Petruska, M. A., Koleske, D. D., Crawford, M. H. & Klimov, V. I. Nanocrystal-based light-emitting diodes utilizing high-efficiency nonradiative energy transfer for color conversion. *Nano Lett.* **6**, 1396–1400 (2006).
19. Prins, F., Goodman, A. J. & Tisdale, W. A. Reduced dielectric screening and enhanced energy transfer in single- and few-layer MoS_2. *Nano Lett.* **14**, 6087–6091 (2014).
20. Mehlenbacher, R. D. et al. Energy transfer pathways in semiconducting carbon nanotubes revealed using two-dimensional white-light spectroscopy. *Nat. Commun.* **6**, 1–7 (2015).
21. Prasai, D. et al. Electrical control of near-field energy transfer between quantum dots and two-dimensional semiconductors. *Nano Lett.* **15**, 4374–4380 (2015).
22. Federspiel, F. et al. Distance dependence of the energy transfer rate from a single semiconductor nanostructure to graphene. *Nano Lett.* **15**, 1252–1258 (2015).
23. Olutas, M., Guzelturk, B., Kelestemur, Y., Gungor, K. & Demir, H. V. Highly efficient nonradiative energy transfer from colloidal semiconductor quantum dots to wells for sensitive noncontact temperature probing. *Adv. Funct. Mater.* **26**, 2891–2899 (2016).
24. Raja, A. et al. Energy transfer from quantum dots to graphene and MoS_2: the role of absorption and screening in two-dimensional materials. *Nano Lett.* **16**, 2328–2333 (2016).
25. Zang, H. et al. Nonradiative energy transfer from individual CdSe/ZnS quantum dots to single-layer and few-layer tin disulfide. *ACS Nano* **10**, 4790–4796 (2016).
26. Gough, J. J. et al. Dependence of photocurrent enhancements in quantum dot (QD)-sensitized MoS_2 devices on MoS_2 film properties. *Adv. Funct. Mater.* **28**, 1706149 (2018).
27. Goodfellow, K. M. et al. Distance-dependent energy transfer between CdSe/CdS quantum dots and a two-dimensional semiconductor. *Appl. Phys. Lett.* **108**, 021101 (2016).
28. Erdem, O. et al. Orientation-controlled nonradiative energy transfer to colloidal nanoplatelets: engineering dipole orientation factor. *Nano Lett.* **19**, 4297–4305 (2019).
29. Liu, H., Wang, T., Wang, C., Liu, D. & Luo, J. Exciton radiative recombination dynamics and nonradiative energy transfer in two-dimensional transition-metal dichalcogenides. *J. Phys. Chem. C* **123**, 10087–10093 (2019).
30. Liu, H. et al. Controllable interlayer charge and energy transfer in perovskite quantum dots/ transition metal dichalcogenide heterostructures. *Adv. Mater. Interfaces* **6**, 1901263 (2019).
31. Flach, J. T., Wang, J., Arnold, M. S. & Zanni, M. T. Providing time to transfer: longer lifetimes lead to improved energy transfer in films of semiconducting carbon nanotubes. *J. Phys. Chem. Lett.* **11**, 6016–6024 (2020).
32. Zhang, Q., Linardy, E., Wang, X. & Eda, G. Excitonic energy transfer in heterostructures of quasi-2D perovskite and monolayer WS_2. *ACS Nano* **14**, 11482–11489 (2020).
33. Zhou, H. et al. Controlling exciton and valley dynamics in two-dimensional heterostructures with atomically precise interlayer proximity. *ACS Nano* **14**, 4618–4625 (2020).
34. Zhang, C. et al. Near-unity-efficiency energy transfer from perovskite to monolayer semiconductor through long-range migration and asymmetric interfacial transfer. *ACS Appl. Mater. Interfaces* **13**, 41895–41903 (2021).
35. Karpińska, M. et al. Nonradiative energy transfer and selective charge transfer in a $WS_2/(PEA)_2PbI_4$ heterostructure. *ACS Appl. Mater. Interfaces* **13**, 33677–33684 (2021).
36. Tumiel, T. M., Amin, M. & Krauss, T. D. Single-walled carbon nanotube dark exciton photoluminescence dynamics. *J. Phys. Chem. C* **125**, 25022–25029 (2021).
37. Padgaonkar, S. et al. Mechanism of long-range energy transfer from quantum dots to black phosphorus. *J. Phys. Chem. C* **125**, 15458–15464 (2021).
38. Wieland, L., Li, H., Rust, C., Chen, J. & Flavel, B. S. Carbon nanotubes for photovoltaics: from lab to industry. *Adv. Energy Mater.* **11**, 2002880 (2021).
39. Bradac, C., Xu, Z.-Q. & Aharonovich, I. Quantum energy and charge transfer at two-dimensional interfaces. *Nano Lett.* **21**, 1193–1204 (2021).
40. Zhang, X., Leng, X., Yin, H. & Ma, Y. Role of dark excitons in the excitation energy transfer of carbon nanotubes. *J. Phys. Chem. C* **125**, 17861–17869 (2021).
41. Mak, K. F., Lee, C., Hone, J., Shan, J. & Heinz, T. F. Atomically thin MoS_2: a new direct-gap semiconductor. *Phys. Rev. Lett.* **105**, 136805 (2010).
42. Bernardi, M., Palummo, M. & Grossman, J. C. Extraordinary sunlight absorption and one nanometer thick photovoltaics using two-dimensional monolayer materials. *Nano Lett.* **13**, 3664–3670 (2013).
43. Amani, M. et al. Near-unity photoluminescence quantum yield in MoS_2. *Science* **350**, 1065–1068 (2015).
44. Mak, K. F. & Shan, J. Photonics and optoelectronics of 2D semiconductor transition metal dichalcogenides. *Nat. Photonics* **10**, 216–226 (2016).
45. Lundt, N. et al. Room-temperature Tamm-plasmon exciton-polaritons with a WSe_2 monolayer. *Nat. Commun.* **7**, 1–6 (2016).
46. Manzeli, S., Ovchinnikov, D., Pasquier, D., Yazyev, O. V. & Kis, A. 2D transition metal dichalcogenides. *Nat. Rev. Mater.* **2**, 1–15 (2017).
47. Liu, X. et al. Control of coherently coupled exciton polaritons in monolayer tungsten disulphide. *Phys. Rev. Lett.* **119**, 027403 (2017).
48. Wang, G. et al. Colloquium: excitons in atomically thin transition metal dichalcogenides. *Rev. Mod. Phys.* **90**, 021001 (2018).
49. Mueller, T. & Malic, E. Exciton physics and device application of two-dimensional transition metal dichalcogenide semiconductors. *npj 2D Mater. Appl.* **2**, 1–12 (2018).
50. Wilson, N. P., Yao, W., Shan, J. & Xu, X. Excitons and emergent quantum phenomena in stacked 2D semiconductors. *Nature* **599**, 383–392 (2021).
51. Ramasubramaniam, A. Large excitonic effects in monolayers of molybdenum and tungsten dichalcogenides. *Phys. Rev. B* **86**, 115409 (2012).
52. Qiu, D. Y., da Jornada, F. H. & Louie, S. G. Optical spectrum of MoS_2: many-body effects and diversity of exciton states. *Phys. Rev. Lett.* **111**, 216805 (2013).
53. Chernikov, A. et al. Exciton binding energy and nonhydrogenic Rydberg series in monolayer WS_2. *Phys. Rev. Lett.* **113**, 076802 (2014).
54. He, K. et al. Tightly bound excitons in monolayer WSe_2. *Phys. Rev. Lett.* **113**, 026803 (2014).
55. Kozawa, D. et al. Evidence for fast interlayer energy transfer in $MoSe_2/WS_2$ heterostructures. *Nano Lett.* **16**, 4087–4093 (2016).
56. Taghipour, N. et al. Near-unity efficiency energy transfer from colloidal semiconductor quantum wells of CdSe/CdS nanoplatelets to a monolayer of MoS_2. *ACS Nano* **12**, 8547–8554 (2018).
57. Wu, L., Chen, Y., Zhou, H. & Zhu, H. Ultrafast energy transfer of both bright and dark excitons in 2D van der Waals heterostructures beyond dipolar coupling. *ACS Nano* **13**, 2341–2348 (2019).
58. Tomita, A., Shah, J. & Knox, R. S. Efficient exciton energy transfer between widely separated quantum wells at low temperatures. *Phys. Rev. B* **53**, 10793–10803 (1996).
59. Lyo, S. K. Energy transfer of excitons between quantum wells separated by a wide barrier. *Phys. Rev. B* **62**, 13641–13656 (2000).
60. Swathi, R. S. & Sebastian, K. L. Long range resonance energy transfer from a dye molecule to graphene has (distance)-4 dependence. *J. Chem. Phys.* **130**, 086101 (2009).
61. Swathi, R. & Sebastian, K. Distance dependence of fluorescence resonance energy transfer. *J. Chem. Sci.* **121**, 777–787 (2009).
62. Malic, E., Appel, H., Hofmann, O. T. & Rubio, A. Förster-induced energy transfer in functionalized graphene. *J. Phys. Chem. C* **118**, 9283–9289 (2014).
63. Selig, M., Malic, E., Ahn, K. J., Koch, N. & Knorr, A. Theory of optically induced Förster coupling in van der Waals coupled heterostructures. *Phys. Rev. B* **99**, 035420 (2019).
64. Katzer, M. et al. Impact of dark excitons on Förster-type resonant energy transfer between dye molecules and atomically thin semiconductors. *Phys. Rev. B* **107**, 035304 (2023).
65. Zhang, X.-X. et al. Magnetic brightening and control of dark excitons in monolayer WSe_2. *Nat. Nanotechnol.* **12**, 883–888 (2017).
66. Robert, C. et al. Measurement of the spin-forbidden dark excitons in MoS_2 and $MoSe_2$ monolayers. *Nat. Commun.* **11**, 1–8 (2020).

67. Wang, G. et al. In-plane propagation of light in transition metal dichalcogenide monolayers: optical selection rules. *Phys. Rev. Lett.* **119**, 047401 (2017).
68. Li, Z. et al. Revealing the biexciton and trion-exciton complexes in BN encapsulated WSe_2. *Nat. Commun.* **9**, 3719 (2018).
69. Peng, G.-H. et al. Distinctive signatures of the spin- and momentum-forbidden dark exciton states in the photoluminescence of strained WSe_2 monolayers under thermalization. *Nano Lett.* **19**, 2299–2312 (2019).
70. Malic, E. et al. Dark excitons in transition metal dichalcogenides. *Phys. Rev. Mater.* **2**, 014002 (2018).
71. Selig, M. et al. Dark and bright exciton formation, thermalization, and photoluminescence in monolayer transition metal dichalcogenides. *2D Mater.* **5**, 035017 (2018).
72. Bao, D. et al. Probing momentum-indirect excitons by near-resonance photoluminescence excitation spectroscopy in WS_2 monolayer. *2D Mater.* **7**, 031002 (2020).
73. Deilmann, T. & Thygesen, K. S. Finite-momentum exciton landscape in mono- and bilayer transition metal dichalcogenides. *2D Mater.* **6**, 035003 (2019).
74. Liu, E. et al. Multipath optical recombination of intervalley dark excitons and trions in monolayer WSe_2. *Phys. Rev. Lett.* **124**, 196802 (2020).
75. Qiu, D. Y., Cao, T. & Louie, S. G. Nonanalyticity, valley quantum phases, and lightlike exciton dispersion in monolayer transition metal dichalcogenides: theory and first-principles calculations. *Phys. Rev. Lett.* **115**, 176801 (2015).
76. Lo, P.-Y., Peng, G.-H., Li, W.-H., Yang, Y. & Cheng, S.-J. Full-zone valley polarization landscape of finite-momentum exciton in transition metal dichalcogenide monolayers. *Phys. Rev. Res.* **3**, 043198 (2021).
77. Splendiani, A. et al. Emerging photoluminescence in monolayer MoS_2. *Nano Lett.* **10**, 1271–1275 (2010).
78. Xiao, D., Liu, G.-B., Feng, W., Xu, X. & Yao, W. Coupled spin and valley physics in monolayers of MoS_2 and other group-vi dichalcogenides. *Phys. Rev. Lett.* **108**, 196802 (2012).
79. Zeng, H., Dai, J., Yao, W., Xiao, D. & Cui, X. Valley polarization in MoS_2 monolayers by optical pumping. *Nat. Nanotechnol.* **7**, 490–493 (2012).
80. Seyler, K. L. et al. Electrical control of second-harmonic generation in a WSe_2 monolayer transistor. *Nat. Nanotechnol.* **10**, 407–411 (2015).
81. Kadantsev, E. S. & Hawrylak, P. Electronic structure of a single MoS_2 monolayer. *Solid State Commun.* **152**, 909–913 (2012).
82. Wu, F., Qu, F. & MacDonald, A. H. Exciton band structure of monolayer MoS_2. *Phys. Rev. B* **91**, 075310 (2015).
83. Qiu, D. Y., da Jornada, F. H. & Louie, S. G. Screening and many-body effects in two-dimensional crystals: monolayer MoS_2. *Phys. Rev. B* **93**, 235435 (2016).
84. Winther, K. T. & Thygesen, K. S. Band structure engineering in van der Waals heterostructures via dielectric screening: the gδw method. *2D Mater.* **4**, 025059 (2017).
85. Ross, J. S. et al. Electrical control of neutral and charged excitons in a monolayer semiconductor. *Nat. Commun.* **4**, 1–6 (2013).
86. Li, Y. et al. Measurement of the optical dielectric function of monolayer transition-metal dichalcogenides: MoS_2, $MoSe_2$, WS_2, and WSe_2. *Phys. Rev. B* **90**, 205422 (2014).
87. Ye, Z. et al. Probing excitonic dark states in single-layer tungsten disulphide. *Nature* **513**, 214–218 (2014).
88. Wang, G. et al. Giant enhancement of the optical second-harmonic emission of WSe_2 monolayers by laser excitation at exciton resonances. *Phys. Rev. Lett.* **114**, 097403 (2015).
89. Bastard, G., Mendez, E. E., Chang, L. L. & Esaki, L. Exciton binding energy in quantum wells. *Phys. Rev. B* **26**, 1974–1979 (1982).
90. Weisbuch, C., Benisty, H. & Houdré, R. Overview of fundamentals and applications of electrons, excitons and photons in confined structures. *J. Lumin.* **85**, 271–293 (2000).
91. Ardizzone, V. et al. Emerging 2D materials for room-temperature polaritonics. *Nanophotonics* **8**, 1547–1558 (2019).
92. Yu, H., Liu, G.-B., Gong, P., Xu, X. & Yao, W. Dirac cones and Dirac saddle points of bright excitons in monolayer transition metal dichalcogenides. *Nat. Commun.* **5**, 1–7 (2014).
93. Sham, L. J. & Rice, T. M. Many-particle derivation of the effective-mass equation for the Wannier exciton. *Phys. Rev.* **144**, 708–714 (1966).
94. Hanke, W. & Sham, L. J. Many-particle effects in the optical spectrum of a semiconductor. *Phys. Rev. B* **21**, 4656–4673 (1980).
95. Rohlfing, M. & Louie, S. G. Electron-hole excitations in semiconductors and insulators. *Phys. Rev. Lett.* **81**, 2312–2315 (1998).
96. Bieniek, M., Szulakowska, L. & Hawrylak, P. Band nesting and exciton spectrum in monolayer MoS_2. *Phys. Rev. B* **101**, 125423 (2020).
97. Trolle, M. L., Pedersen, T. G. & Véniard, V. Model dielectric function for 2D semiconductors including substrate screening. *Sci. Rep.* **7**, 39844 (2017).
98. Florian, M. et al. The dielectric impact of layer distances on exciton and trion binding energies in van der Waals heterostructures. *Nano Lett.* **18**, 2725–2732 (2018).
99. Kamban, H. C., Pedersen, T. G. & Peres, N. M. R. Anisotropic stark shift, field-induced dissociation, and electroabsorption of excitons in phosphorene. *Phys. Rev. B* **102**, 115305 (2020).
100. Kornyshev, A. A., Rubinshtein, A. I. & Vorotyntsev, M. A. Model nonlocal electrostatics. i. *J. Phys. C Solid State Phys.* **11**, 3307 (1978).
101. Li, W.-H. et al. The key role of non-local screening in the environment-insensitive exciton fine structures of transition-metal dichalcogenide monolayers. *Nanomaterials* **13**, 1739 (2023).
102. Yang, M. et al. Relaxation and darkening of excitonic complexes in electrostatically doped monolayer WSe_2: roles of exciton-electron and trion-electron interactions. *Phys. Rev. B* **105**, 085302 (2022).
103. Li, P. et al. Intervalley electron-hole exchange interaction and impurity-assisted recombination of indirect excitons in WS_2 and WSe_2 monolayers. *Phys. Rev. B* **106**, 085414 (2022).
104. Parfitt, D. G. W. & Portnoi, M. E. The two-dimensional hydrogen atom revisited. *J. Math. Phys.* **43**, 4681–4691 (2002).
105. Shibuya, T.-i & Wulfman, C. E. The Kepler problem in two-dimensional momentum space. *Am. J. Phys.* **33**, 570–574 (1965).
106. Qiu, D. Y., Cohen, G., Novichkova, D. & Refaely-Abramson, S. Signatures of dimensionality and symmetry in exciton band structure: consequences for exciton dynamics and transport. *Nano Lett.* **21**, 7644–7650 (2021).
107. Grosso, G. & Parravicini, G. *Solid State Physics* (Elsevier, 2000).
108. Harrison, P. & Valavanis, A. *Quantum Wells, Wires and Dots: Theoretical and Computational Physics of Semiconductor Nanostructures* (Wiley, 2016).
109. Jorda, S., Rössler, U. & Broido, D. Fine structure of excitons and polariton dispersion in quantum wells. *Phys. Rev. B* **48**, 1669–1677 (1993).
110. Kuhn, H. Classical aspects of energy transfer in molecular systems. *J. Chem. Phys.* **53**, 101–108 (1970).
111. Persson, B. N. J. & Lang, N. D. Electron-hole-pair quenching of excited states near a metal. *Phys. Rev. B* **26**, 5409–5415 (1982).
112. Barnes, W. L. Fluorescence near interfaces: the role of photonic mode density. *J. Mod. Opt.* **45**, 661–699 (1998).
113. Basko, D., La Rocca, G., Bassani, F. & Agranovich, V. Förster energy transfer from a semiconductor quantum well to an organic material overlayer. *Eur. Phys. J. B* **8**, 353–362 (1999).
114. Kim, D., Okahara, S., Nakayama, M. & Shim, Y. Experimental verification of Förster energy transfer between semiconductor quantum dots. *Phys. Rev. B* **78**, 153301 (2008).
115. Gordon, J. & Gartstein, Y. N. Dielectric polarization, anisotropy and nonradiative energy transfer into nanometre-scale thin semiconducting films. *J. Phys. Condens. Matter* **25**, 425302 (2013).
116. Rindermann, J. J. et al. Dependence of resonance energy transfer on exciton dimensionality. *Phys. Rev. Lett.* **107**, 236805 (2011).
117. Kresse, G. & Furthmüller, J. Efficient iterative schemes for ab initio total-energy calculations using a plane-wave basis set. *Phys. Rev. B* **54**, 11169–11186 (1996).
118. Perdew, J. P., Burke, K. & Ernzerhof, M. Generalized gradient approximation made simple. *Phys. Rev. Lett.* **77**, 3865–3868 (1996).
119. Krukau, A. V., Vydrov, O. A., Izmaylov, A. F. & Scuseria, G. E. Influence of the exchange screening parameter on the performance of screened hybrid functionals. *J. Chem. Phys.* **125**, 224106 (2006).
120. Mostofi, A. A. et al. An updated version of wannier90: a tool for obtaining maximally-localised Wannier functions. *Comput. Phys. Commun.* **185**, 2309–2310 (2014).
121. Mostofi, A. A. et al. wannier90: a tool for obtaining maximally-localised Wannier functions. *Comput. Phys. Commun.* **178**, 685–699 (2008).
122. Peng, G.-H., Sanchez, O. J. G., Li, W.-H., Lo, P.-Y. & Cheng, S.-J. Tailoring the superposition of finite-momentum valley exciton states in transition-metal dichalcogenide monolayers by using polarized twisted light. *Phys. Rev. B* **106**, 155304 (2022).
123. Zahid, F., Liu, L., Zhu, Y., Wang, J. & Guo, H. A generic tight-binding model for monolayer, bilayer and bulk MoS_2. *AIP Adv.* **3**, 052111 (2013).
124. Debnath, B., Barlas, Y., Wickramaratne, D., Neupane, M. R. & Lake, R. K. Exciton condensate in bilayer transition metal dichalcogenides: strong coupling regime. *Phys. Rev. B* **96**, 174504 (2017).
125. Ridolfi, E., Le, D., Rahman, T. S., Mucciolo, E. R. & Lewenkopf, C. H. A tight-binding model for MoS_2 monolayers. *J. Phys. Condens. Matter* **27**, 365501 (2015).
126. Wang, G. et al. Exciton states in monolayer $MoSe_2$: impact on interband transitions. *2D Mater.* **2**, 045005 (2015).
127. Efros, A. L. et al. Band-edge exciton in quantum dots of semiconductors with a degenerate valence band: dark and bright exciton states. *Phys. Rev. B* **54**, 4843–4856 (1996).

128. Ekimov, A. I. et al. Absorption and intensity-dependent photoluminescence measurements on CdSe quantum dots: assignment of the first electronic transitions. *J. Opt. Soc. Am. B* **10**, 100–107 (1993).
129. Haug, H. & Koch, S. W. *Quantum Theory of the Optical and Electronic Properties of Semiconductors* (World Scientific, 2009).
130. Simbulan, K. B. et al. Selective photoexcitation of finite-momentum excitons in monolayer MoS_2 by twisted light. *ACS Nano* **15**, 3481–3489 (2021).
131. Peimyoo, N. et al. Engineering dielectric screening for potential-well arrays of excitons in 2D materials. *ACS Appl. Mater. Interfaces* **12**, 55134–55140 (2020).
132. Young, A. F. et al. Electronic compressibility of layer-polarized bilayer graphene. *Phys. Rev. B* **85**, 235458 (2012).
133. Kim, K. K. et al. Synthesis and characterization of hexagonal boron nitride film as a dielectric layer for graphene devices. *ACS Nano* **6**, 8583–8590 (2012).

ACKNOWLEDGEMENTS

This study is supported by the National Science and Technology Council of Taiwan under the contract, MOST 109-2112-M-009-018-MY3, MOST 111-2112-M-A49-014, MOST 110-2112-M-005-002, MOST 111-2123-M-006-001 and by National Center for Theoretical Sciences (NCTS) of Taiwan, and by National Center for High-Performance Computing (NCHC) of Taiwan. The authors are grateful to Chih-Wei Luo, Chun-Liang Lin, and Yu-Chan Tai for fruitful discussions.

AUTHOR CONTRIBUTIONS

S.-J.C. conceived and supervised the project. J.-D.L., P.-Y.L., S.-Y.H., and G.-Y.C. developed the FRET theory. G.-H.P. and W.-H.L. carried out the first-principles computations and calculated the exciton band structures. J.-D.L. and S.-J.C. wrote the paper with input from other authors. All authors participated in discussions and revisions of the manuscript.

COMPETING INTERESTS

The authors declare no competing interests.

ADDITIONAL INFORMATION

Supplementary information The online version contains supplementary material available at https://doi.org/10.1038/s41699-023-00414-z.

Correspondence and requests for materials should be addressed to Shun-Jen Cheng.

Reprints and permission information is available at http://www.nature.com/reprints

Publisher's note Springer Nature remains neutral with regard to jurisdictional claims in published maps and institutional affiliations.